Using Convolutional Neural Network to Determine Time Window for Analyzing Local Shear-Wave Splitting Measurements

Yanwei Zhang*[1,2] and Stephen S. Gao[1]

Abstract

The time window for analyzing local shear-wave splitting (SWS) phases significantly affects the quality of measurements, revealing a noteworthy domain influence. In this study, an approach using convolutional neural network (CNN) is applied to determine the end of time window (*e*), which has a similar idea of the phase-picking CNNs. The start of time window is 0.5 s before *e*. Our data set contains 803 human-labeled measurements, recorded from three stations located in Ridgecrest, California. These measurements are foreshocks and aftershocks of an M 7.1 earthquake on 6 July 2019. After 21 times shifting on each measurement, 90% of the data set is applied as the training data set, with the remaining 10% as the testing data set. The performance of CNN with the testing data set is compared with a nonmachine learning method, multiple filter automatic splitting technique (MFAST). The results reveal that the CNN yields more similar results with human-labeled outcomes than MFAST, as evidenced by lower absolute error and standard deviation for *e*, SWS time, the orientation of fast-wave polarization, and more consistent results on the map. The CNN also performs well when applied to data recorded by a station in Parkfield, California. This study shows the outstanding performance of CNN in picking the time window and the reliable automatic determination of this time window, and it is also a crucial step for future development of automatic ranking methodologies.

Cite this article as Zhang, Y., and S. S. Gao (2024). Using Convolutional Neural Network to Determine Time Window for Analyzing Local Shear-Wave Splitting Measurements, *Seismol. Res. Lett.* **XX**, 1–7, doi: 10.1785/0220230410.

Supplemental Material

Introduction

Seismic anisotropy leads shear waves to turn into two orthogonally polarized waves with distinct velocities, epitomized as shear-wave splitting (SWS; Ando *et al.*, 1980). This SWS reveals as a direct indication of azimuthal anisotropy, quantified by the fast-wave's polarization orientation (ϕ) and the time difference between fast- and slow-wave arrivals (δt) (Silver and Chan, 1991). Different regions of the Earth exhibit heterogeneous conditions leading to SWS due to varying anisotropic properties. In the upper continental crust, previous studies proposed stress-induced anisotropy emerges from fluid-filled microcracks preferentially aligning with the direction of maximum horizontal compressive stress, and structure-induced anisotropy is attributed to fluid-filled fractures adjacent to fault zones, terrane minerals, and sedimentary layering. These anisotropic properties are typically quantified by ϕ and δt of *S* wave from local seismic events (Crampin and Booth, 1985; Cochran *et al.*, 2003, 2020; Crampin and Gao, 2006; Yang *et al.*, 2011; Li and Peng, 2017; Cao *et al.*, 2019; Gao *et al.*, 2019; Jiang *et al.*, 2021; Guzman *et al.*, 2022; Jia, 2022).

Given the focus on local seismic occurrences in these projects, the threshold for minimum magnitude is notably low, resulting in a large number of events within the study area. With rapidly increasing number of stations, there is an exponential surge in the volume of measurements. This increased data set consequently intensifies the time and effort required for manual verification (Jiang *et al.*, 2021; Jia, 2022). Despite significant advancements toward semi- and fully automatic methods of such processes as noted by Gao *et al.* (2006), Peng and Ben-Zion (2004), and Savage *et al.* (2010), manually verified results undeniably present superior quality, enabling more robust and confident analysis of each individual measurement (Jiang *et al.*, 2021; Jia, 2022).

In recent years, applications of machine-learning (ML)-based techniques on various scientific problems have dramatically increased, and over-human performance has been shown in diverse areas (Silver *et al.*, 2016; Linville *et al.*, 2019). Zhang and Gao (2022) developed a convolutional neural network

1. Geology and Geophysics Program, Missouri University of Science and Technology, Rolla, Missouri, U.S.A., https://orcid.org/0000-0003-1809-0174 (YZ); https://orcid.org/0000-0001-7530-7128 (SSG); 2. Kansas Geological Survey, University of Kansas, Lawrence, Kansas, U.S.A.

*Corresponding author: y230z012@ku.edu

© Seismological Society of America

Downloaded from http://pubs.geoscienceworld.org/ssa/srl/article-pdf/doi/10.1785/0220230410/6544270/srl-2023410.1.pdf
by Missouri University of Science and Technology, Stephen Shangxing Gao

TABLE 1
Structure of the Convolutional Neural Network (CNN)

Layers	Length	Depth	Kernel Size	Stride	Activation Function
Input	400	3	–	–	–
Conv-1D	200	64	3	2	LeakyReLU
Conv-1D	100	64	3	2	LeakyReLU
Conv-1D	50	64	3	2	LeakyReLU
Conv-1D	25	64	3	2	LeakyReLU
Conv-1D	13	64	3	2	LeakyReLU
Conv-1D	7	64	3	2	LeakyReLU
Deconv-1D	13	64	3	1	LeakyReLU
Deconv-1D	25	64	3	1	LeakyReLU
Deconv-1D	50	64	3	1	LeakyReLU
Deconv-1D	100	64	3	1	LeakyReLU
Deconv-1D	200	64	3	1	LeakyReLU
Deconv-1D and output	400	1	3	1	Sigmoid

(CNN) to rank SWS measurements of teleseismic (quality and type of measurements) and revealed great potential in this task. Without a precisely determined ending window for the *PKS*, *SKS*, and *SKKS* phases, CNN still delivers results more similar to manual outcomes than non-ML automatic ranking methods (Link *et al.*, 2022; Zhang and Gao, 2022).

For local SWS measurements, due to the narrow time window of the *S* phases, the selection of time windows for analyzing *S* phases profoundly impacts the measurement quality, highlighting a significant domain influence. Without a well-determined time window, subsequent methodologies for calculating splitting parameters, such as the minimum energy method, cannot provide reliable outcomes (Silver and Chan, 1991; Liu and Gao, 2013). Consequently, an automated method for accurately selecting these time windows is essential for the autoranking of local SWS measurements. In this study, we utilize a CNN to determine the end of the time window (*e*), drawing parallels with phase-picking CNN methodologies (Zhu and Beroza, 2019). The exclusive focus on determining the *e* is attributed to its narrow acceptable range. In contrast, the start of the time windows has a broader acceptable range (Peng and Ben-Zion, 2004; Teanby *et al.*, 2004), and for our purposes, we have designated it as 0.5 s before *e*.

Data and Methods

Our study utilizes a data set containing 803 measurements recorded from three broadband stations located in Ridgecrest, California. The active fault network primarily consists of the northwest–southeast-striking Eastern Little Lake fault, the northeast–southwest-striking Southern Little Lake fault, and several additional faults (Jia, 2022). These measurements are from the foreshocks and aftershocks of a magnitude 7.1 earthquake that occurred on 6 July 2019. The measurements are manually picked the time windows of *S* phases and analyzed in Jia (2022), and magnitude varies from 0.0 to 4.9. A 4 s window, centered at the theoretical *S*-wave arrival time with a sampling rate of 0.01 s, is employed to segment three-component seismic records and each measurement is processed using a 0.5–10 Hz band-pass filter. To enhance our data set, each measurement is randomly shifted 20 times in the range of ±0.2 s, resulting in a total of 16,863 measurements, including the original ones (Shorten and Khoshgoftaar, 2019). Recognizing the inherent variability of *e*, a Gaussian distribution is employed as a mask centered around the human-labeled *e*, recognizing that *e* can be defined within a certain range. The same masking technique was previously employed by Zhu and Beroza (2019) to reduce the effects of human mispicking errors. After random shuffling, 90% of the data set is applied as the training data set, with the remaining 10% as the testing data set.

As inspired from previous studies, a 12-layer U-shape CNN is designed to determine the *e* of each measurement (Table 1; Perol *et al.*, 2018; Zhu and Beroza, 2019). The input to the CNN consists of a three-component seismic record, and the output provides the probability of *e* for each individual data sample (Fig. 1). The 1D convolutional layers (Conv-1D) extract and shrink the useful features from the input data set, and the 1D deconvolutional layers (Deconv-1D) expand the information to fit the data shape of the output. The data length is reduced by half after each Conv-1D and doubled after each Deconv-1D. The activation function between each layer is LeakyReLU with a 0.05 negative slope (Maas *et al.*, 2013) and the activation function of output is Sigmoid (Han and Moraga, 1995):

$$\sigma = \frac{1}{1 + e^{-x}}, \tag{1}$$

in which x is the value of each data point. Based on equation (1), the CNN gives a value (σ) from 0 to 1 at each data point, representing the possibility of *e* at each data point.

As each data point can be considered as a binary classification problem, the binary cross-entropy loss is employed as loss function:

$$L = -\frac{1}{n}\sum_{i=1}^{n} y_i \log(p(y_i)) + (1 - y_i)\log(1 - p(y_i))(n = 400), \tag{2}$$

in which n is the number of data points, y is the real mask, and $p(y)$ is the CNN-predicted results. The optimizer is the Adam, a typical gradient descent method in ML (Kingma and Ba, 2014), with a learning rate of 0.001 and an epoch of 10.

Results

After training, the testing data set is employed to assess the performance of our CNN. The *e* is identified at the maximum

Downloaded from http://pubs.geoscienceworld.org/ssa/srl/article-pdf/doi/10.1785/0220230410/6544270/srl-2023410.1.pdf
by Missouri University of Science and Technology, Stephen Shangxing Gao

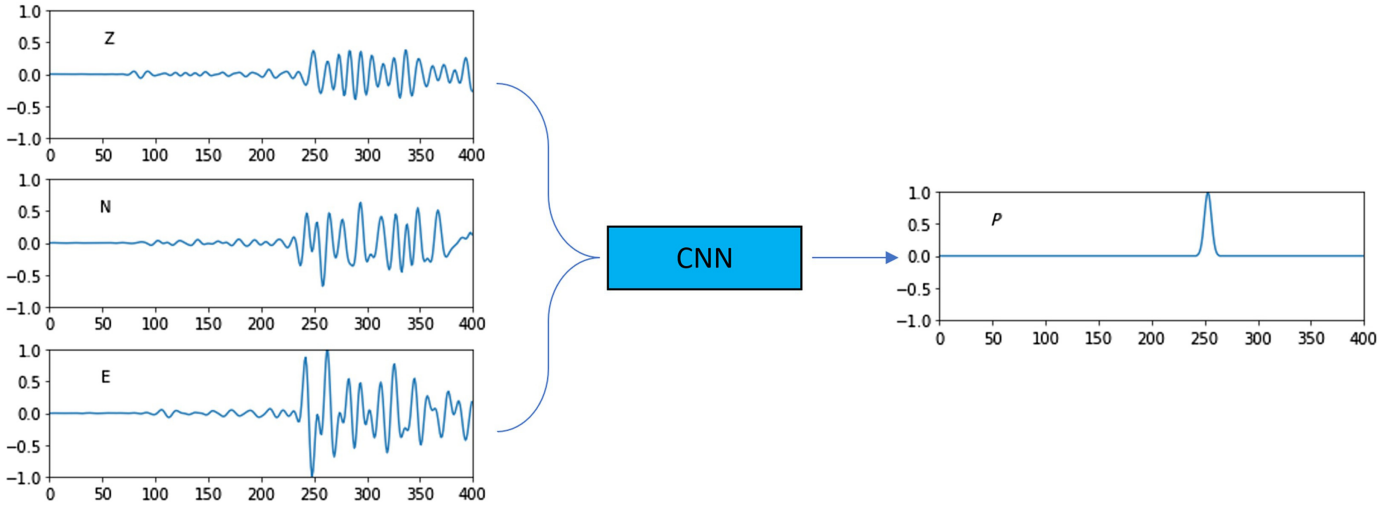

Figure 1. Process of convolutional neural network (CNN). The input is three-component seismic waveforms (Z, N, and E). The output is the probability of *e* at each point (*P*). The color version of this figure is available only in the electronic edition.

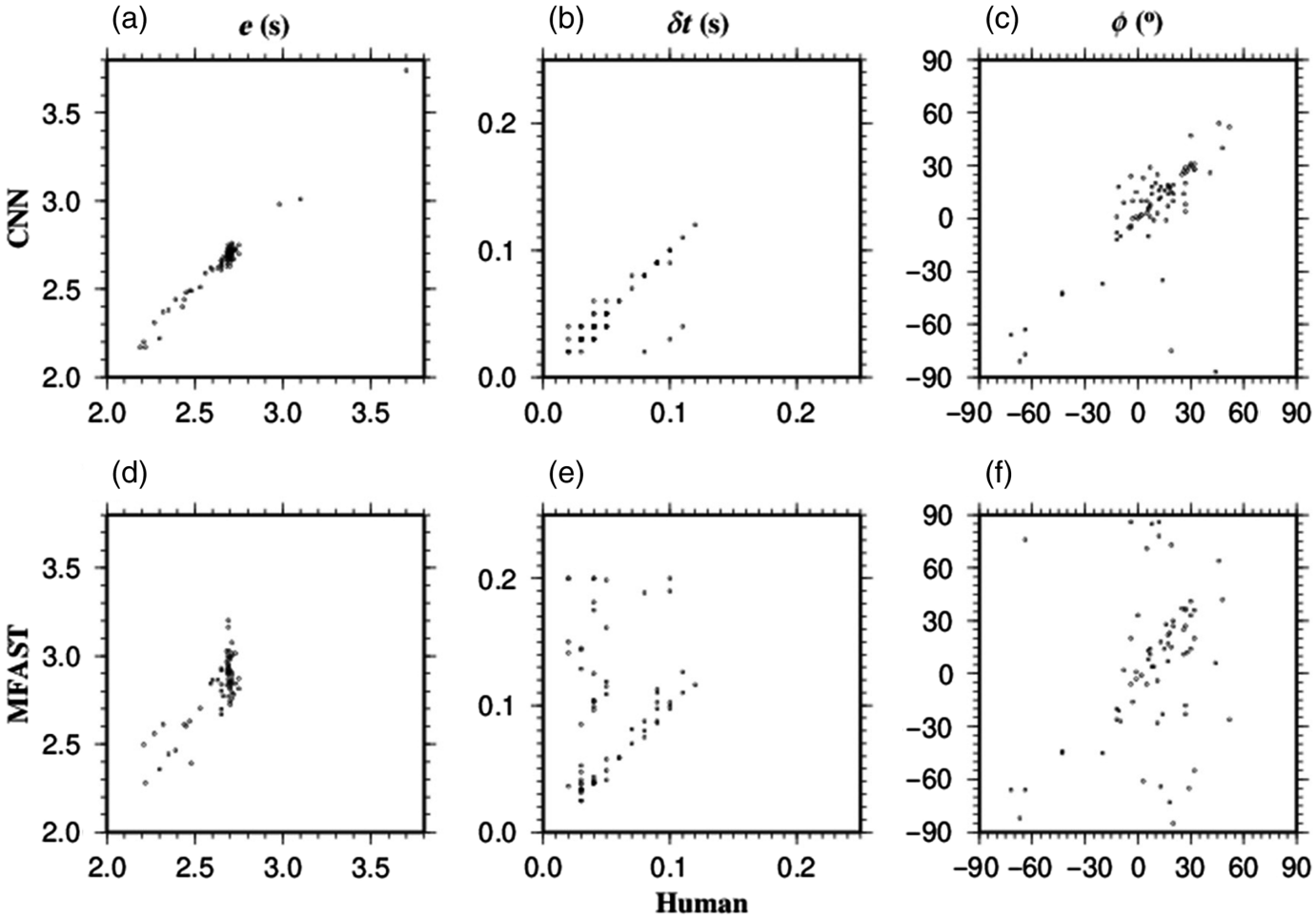

Figure 2. Comparison scatter plot of multiple filter automatic splitting technique (MFAST) and CNN test data set outcomes versus human evaluations. (a,d) Results of *e*. (b,e) Results of δt based on window in panels (a) and (d). (c,f) Results of ϕ based on window in panels (a) and (d).

Downloaded from http://pubs.geoscienceworld.org/ssa/srl/article-pdf/doi/10.1785/0220230410/6544270/srl-2023410.1.pdf
by Missouri University of Science and Technology, Stephen Shangxing Gao

σ of the output, and the start of the time window is set at 0.5 s before e. The technique of minimizing the lesser of the two eigenvalues of the covariance matrix of the seismograms after the correction for anisotropy is employed to calculate the δt and ϕ of each measurement (Silver and Chan, 1991). It simultaneously searches for the two splitting parameters and the polarization orientation of the shear wave. Consequently, the radial and transverse components are calculated relative to the optimal polarization orientation. As revealed in Figures S1 and S2, available in the supplemental material to this article, the measurements processed using the CNN-picked time window display features similar to the A and B quality proposed by Liu and Gao (2013). These include pronounced *S*-wave arrivals on the horizontal components, effective removal of energy on the transverse component, elliptical particle motion patterns in the original measurements that become approximately linear after correction, and a well-defined minimum energy contour on the transverse component. In addition, the measurements exhibit similar features when compared to those based on human-picked time windows.

In Figure 2a–c, the results of the testing data set based on both the CNN- and human-picked time window are plotted to discern their similarity and difference. Remarkably, the CNN mirrors human precision across all parameters: e, δt, and ϕ. The quantitative differences in the results are minimal as well, with average errors of 0.02309 s for e, 0.00519 s for δt, and 8.54321° for ϕ. The SWS measurements serve as a potent tool to analyze spatial anisotropy within the investigation area. Hence, visualizing the distribution of these measurements on a map is necessary. In Figures 3a,e and S3a,b, when the measurements derived for the CNN-picked time window are compared with those from the human-picked time window, a coherent trend emerges. Both sets of results exhibit consistent spatial distribution, further underscoring the accuracy of our CNN in mimicking human precision when plotted across both station and event locations.

Discussion

Comparison with a non-ML method

Over the years, various non-ML techniques have been developed for the fully automated ranking of local SWS measurements (e.g., Peng and Ben-Zion, 2004; Savage *et al.*, 2010). For the purpose of comparative analysis in this research, we choose a widely recognized method, multiple filter automatic splitting technique (MFAST) (v.2.1, do_sta_verylocal, Savage *et al.*, 2010), to compare against the CNN-based approach proposed in this study. Similar to other non-ML methods, MFAST requires measurements with picked *S* arrivals and selects a time window surrounding the *S* arrival time by employing shifting windows (Peng and Ben-Zion, 2004; Savage *et al.*, 2010). To fully automate this process, we leverage PhaseNet (model = "ai4eps/phasenet," Zhu and Beroza, 2019), a prevalent

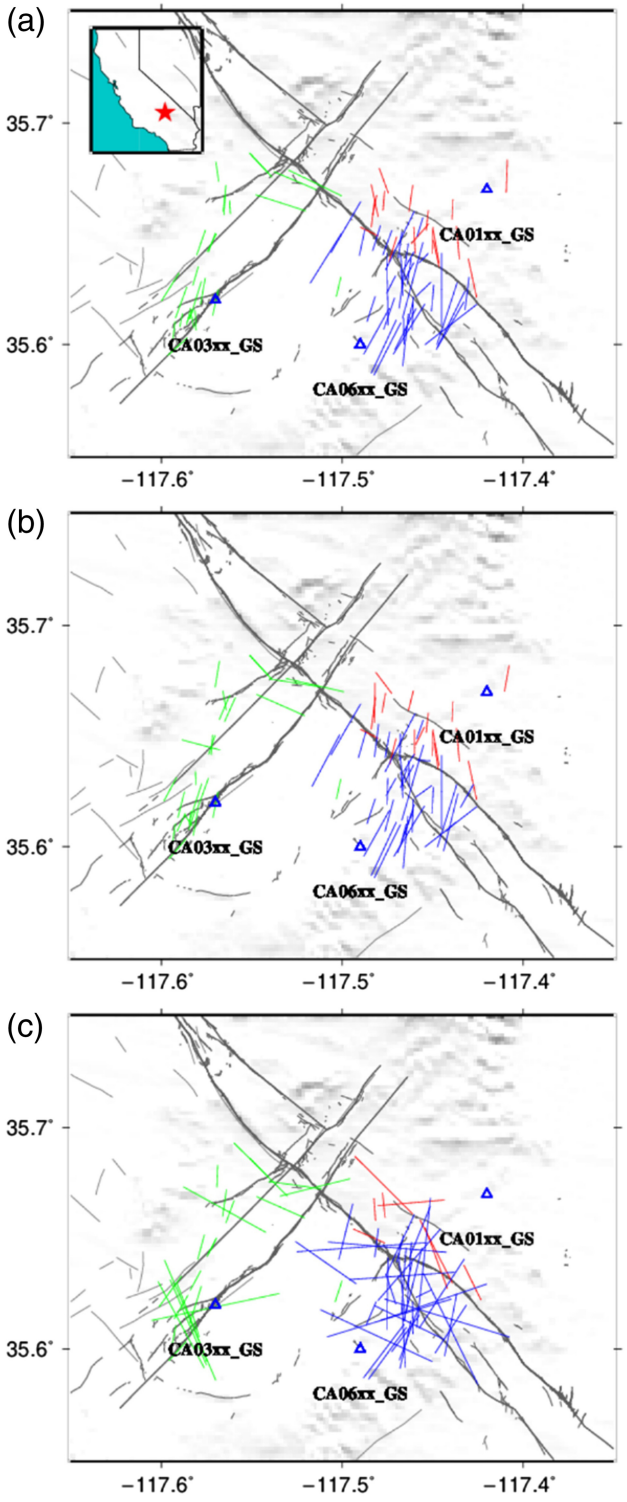

Figure 3. Plotting all measurements in the testing data set at event location. (a) Results based on human-picked time window. (b) Similar to (a) but based on CNN-picked time window. (c) Similar to (a) as well but for MFAST. The red bars are recorded by station CA01xx_GS, the green bars are recorded by station CA03xx_GS, and the blue bars are recorded by station CA06xx_GS. The gray lines are faults. The red star in inset of panel (a) labels the study area in California, United States. The color version of this figure is available only in the electronic edition.

Downloaded from http://pubs.geoscienceworld.org/ssa/srl/article-pdf/doi/10.1785/0220230410/6544270/srl-2023410.1.pdf
by Missouri University of Science and Technology, Stephen Shangxing Gao

ML-based approach for phase picking, to initially discern the *S* arrival time. Utilizing a threshold value of 0.50, PhaseNet successfully picks 70 measurements in the testing data set, and then MFAST selects the time window based on PhaseNet's outcomes. MFAST uses a broader band-pass frequency range (e.g., 1–8, 1–15, and 1–30 Hz) than ours. However, all the frequency ranges used by MFAST and this study include the vast majority of the shear-wave energy; therefore, the difference in frequency bands is unlikely leading to a biased comparison. For optimal performance, the best band-pass filter, determined by MFAST, is utilized rather than employing a fixed filter used in the CNN. To ensure inclusion of all measurements, the signal-to-noise ratio threshold is set to 0 for MFAST; otherwise, with the default threshold of 2.0, only seven measurements from the test data set are selected. Finally, MFAST still rejects one measurement and picks the time window for 69 measurements.

As with earlier comparisons, the results of MFAST against with human's outcome are illustrated in Figure 2d–f. The distribution of these results exhibits greater dispersion than outcomes derived from the CNN. Additionally, the quantitative differences are more pronounced, with average errors of 0.197 s for e, 0.043 s for δt, and 24.174° for ϕ. When mapping the measurements based on the MFAST-picked window, Figure 3 and Figure S3 makes it evident that measurements leveraging the CNN-picked window align more consistently and bear a closer resemblance to the human-picked results.

Application to data from Parkfield, California

Because of the lack of human-labeled data sets in local SWS measurements, the data recorded by station BURN (network code: YH) in Parkfield, California, are manually checked to evaluate the performance of CNN. The station is a part of the Parkfield Area Seismic Observatory array. The main purpose of this array is to enhance the precision in pinpointing the locations of Microearthquake along the San Andreas faults. Ultimately, 302 good measurements are obtained using manually selected time windows of the *S* phase. The CNN is then applied to determine the e values for these measurements, and the associated splitting parameters are calculated (Fig. S4). The results derived from both human and the CNN are visualized on a map as well. As depicted in Figure 4 and Figure S5, the results of CNN exhibit a high degree of consistency with human results, distinguished only by minimal discrepancies. The station averaged δt and ϕ from human analyses are 0.045 ± 0.010 s and 166.414 ± 22.737°, respectively. For CNN, they are 0.046 ± 0.013 s and 165.424 ± 21.126°, respectively. These findings are also consistent with those of a previous study, which reported a δt of 0.053 ± 0.053 s and a ϕ of 174° (Liu *et al.*, 2008).

Start of time window

Although the start of the time window offers a broader acceptable range, it retains significant influence in removing interference of *P* and *P*-coda waves while ensuring that the entirety of the *S* phases is captured. In our study, a selection of 0.5 s before e is made based on a thorough empirical examination of all measurements. This choice proves to be compatible with all the measurements in the testing data set.

Nevertheless, it is essential that an optimal start of the time window is better varying based on the specific attributes of individual measurements, especially the depth of event and the distance between event and station. Within our data set, event depths range from 3.1 to 14.4 km, and distance between events and stations range from 0.7 to 14.1 km with the

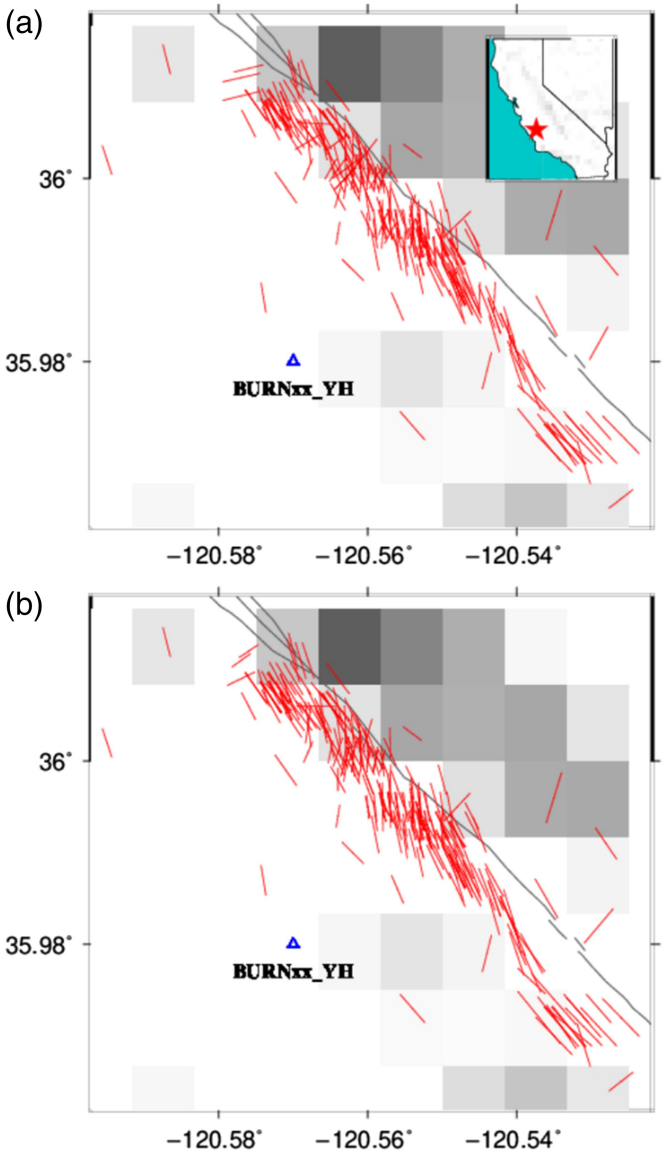

Figure 4. Same as Figure 3 but for measurements from station BURNxx_YH. The measurements are plotted at the event epicenters. (a) Results obtained based on human-picked time windows. The gray lines are faults, and the red star in the inset map labels the study area in California, United States. (b) Results obtained based on CNN-picked time windows. The color version of this figure is available only in the electronic edition.

Downloaded from http://pubs.geoscienceworld.org/ssa/srl/article-pdf/doi/10.1785/0220230410/6544270/srl-2023410.1.pdf
by Missouri University of Science and Technology, Stephen Shangxing Gao

maximum incident angle approximately 35°. For shallower and closer events, the start of the time window should be closer to *e* to negate the impacts of *P* and *P*-coda waves. Conversely, for events with greater depth and distance, the start of the time window ought to be distanced further from *e*, ensuring the complete capture of the *S* phases.

Fully automatic ranking measurements with ML

The precise determination of the *S* phase time window plays an important role in ensuring the quality of measurements. This precision directly impacts the reliability of the splitting parameters (δt and ϕ) associated with those measurements. Notably, energy minimization on the corrected transverse component when using an accurate time window serves as a clear feature that can be beneficial for future ML-based automatic ranking approaches (Liu and Gao, 2013; Zhang and Gao, 2022). After accumulating more measurements, and once a reliable time window is applied, another CNN can be designed for ranking the measurements. Drawing parallels with the approach of Zhang and Gao (2022), the input of CNN can comprise the original and corrected radial and transverse components, whereas the output can be the possibility of measurements being acceptable.

Conclusions

In this study, a CNN is developed specifically for picking *e*, the end of the time window for local SWS measurements, with that start of time window set at 0.5 s before *e*. Utilizing a published human-labeled data set as our benchmark (Jia, 2022), we trained and tested the CNN, using data from a different area to evaluate its performance. Our findings underscore that the outcomes derived from the CNN closely mirror the results of human and outperform traditional non-ML approach. The CNN exhibits lower average errors across δt and ϕ. This robust performance accentuates the potential of CNN on this task. The accurate determination of the *S* phase time window facilitates experts' precision and efficiency in manually ranking local SWS measurements and also lays foundational groundwork for a future fully automated ML-based measuring and ranking system for SWS parameters.

Data and Resources

The code and trained models utilized in this study can be accessed at GitHub (https://github.com/YW-Zhang94/CNN_Local_SWS_f), and the data sets are available at Figshare (https://figshare.com/articles/dataset/CNN_Local_SWS_f/24714855). Both websites were last accessed in December 2023. The supplemental material for this article includes examples of measurements for comparing the outcomes obtained by humans and those generated by the CNN.

Declaration of Competing Interests

The authors acknowledge that there are no conflicts of interest recorded.

Acknowledgments

The authors extend their sincere appreciation to the High-Performance Computing Center at Missouri University of Science and Technology. Special thanks are given to the system administrators of Foundry, the Linux cluster that was obtained through a Major Research Instrumentation grant (Grant Number 1919789). Furthermore, the authors would like to acknowledge contributions of ChatGPT in refining the article.

References

Ando, M., Y. Ishikawa, and H. Wada (1980). S-wave anisotropy in the upper mantle under a volcanic area in Japan, *Nature* **286,** no. 5768, 43–46, doi: 10.1038/286043a0.

Cao, L., H. Kao, K. Wang, C. Chen, J. Mori, S. Ohmi, and Y. Gao (2019). Spatiotemporal variation of crustal anisotropy in the source area of the 2004 Niigata, Japan earthquake, *Bull. Seismol. Soc. Am.* **109,** no. 4, 1331–1342, doi: 10.1785/0120180195.

Cochran, E. S., R. J. Skoumal, D. McPhillips, Z. E. Ross, and K. M. Keranen (2020). Activation of optimally and unfavourably oriented faults in a uniform local stress field during the 2011 Prague, Oklahoma, sequence, *Geophys. J. Int.* **222,** no. 1, 153–168, doi: 10.1093/gji/ggaa153.

Cochran, E. S., J. E. Vidale, and Y. G. Li (2003). Near-fault anisotropy following the Hector Mine earthquake, *J. Geophys. Res.* **108,** no. B9, doi: 10.1029/2002JB002352.

Crampin, S., and D. C. Booth (1985). Shear-wave polarizations near the North Anatolian Fault–II. Interpretation in terms of crack-induced anisotropy, *Geophys. J. Int.* **83,** no. 1, 75–92, doi: 10.1111/j.1365-246X.1985.tb05157.x.

Crampin, S., and Y. Gao (2006). A review of techniques for measuring seismic shear-wave splitting above small earthquakes, *Phys. Earth Planet. In.* **159,** no. 1, 1–14, doi: 10.1016/j.pepi.2006.06.002.

Gao, Y., A. Chen, Y. Shi, Z. Zhang, and L. Liu (2019). Preliminary analysis of crustal shear-wave splitting in the Sanjiang lateral collision zone of the southeast margin of the Tibetan Plateau and its tectonic implications, *Geophys. Prospect.* **67,** 2432–2449, doi: 10.1111/1365-2478.12870.

Gao, Y., P. Hao, and S. Crampin (2006). SWAS: A shear-wave analysis system for semi-automatic measurement of seismic shear-wave splitting above small earthquakes, *Phys. Earth Planet. In.* **159,** no. 1, 71–89, doi: 10.1016/j.pepi.2006.06.003.

Guzman, V., A. Li, and A. Savvaidis (2022). Stress variations in the Delaware Basin from shear-wave splitting analysis, *Seismol. Res. Lett.* **93,** no. 6, 3433–3443, doi: 10.1785/0220220118.

Han, J., and C. Moraga (1995). The influence of the sigmoid function parameters on the speed of backpropagation learning, *International Workshop on Artificial Neural Networks*, Berlin, Heidelberg, Springer Berlin Heidelberg, 195–201, doi: 10.1007/3-540-59497-3_175.

Jia, Y. (2022). Laterally heterogeneous seismic anisotropy investigated by shear wave splitting analyses, *ProQuest Dissertations*, Theses Global (2792820363).

Jiang, E., K. H. Liu, Y. Gao, X. Fu, and S. S. Gao (2021). Spatial variations of upper crustal anisotropy along the San Jacinto Fault Zone in Southern California: Constraints from shear wave splitting analysis, *J. Geophys. Res.* **126,** no. 4, e2020JB020876, doi: 10.1029/2020JB020876.

Downloaded from http://pubs.geoscienceworld.org/ssa/srl/article-pdf/doi/10.1785/0220230410/6544270/srl-2023410.1.pdf
by Missouri University of Science and Technology, Stephen Shangxing Gao

Kingma, D. P., and J. Ba (2014). Adam: A method for stochastic optimization, doi: 10.48550/arXiv.1412.6980.

Li, Z., and Z. Peng (2017). Stress-and structure-induced anisotropy in southern California from two decades of shear wave splitting measurements, *Geophys. Res. Lett.* **44,** no. 19, 9607–9614, doi: 10.1002/2017GL075163.

Link, F., M. C. Reiss, and G. Rümpker (2022). An automatized XKS-splitting procedure for large data sets: Extension package for SplitRacer and application to the USArray, *Comput. Geosci.* **158,** 104961, doi: 10.1016/j.cageo.2021.104961.

Linville, L., K. Pankow, and T. Draelos (2019). Deep learning models augment analyst decisions for event discrimination, *Geophys. Res. Lett.* **46,** no. 7, 3643–3651, doi: 10.1029/2018GL081119.

Liu, K. H., and S. S. Gao (2013). Making reliable shear-wave splitting measurements, *Bull. Seismol. Soc. Am.* **103,** no. 5, 2680–2693, doi: 10.1785/0120120355.

Liu, Y., H. Zhang, C. Thurber, and S. Roecker (2008). Shear wave anisotropy in the crust around the San Andreas fault near Parkfield: Spatial and temporal analysis, *Geophys. J. Int.* **172,** no. 3, 957–970, doi: 10.1111/j.1365-246X.2007.03618.x.

Maas, A. L., A. Y. Hannun, and A. Y. Ng (2013). Rectifier nonlinearities improve neural network acoustic models, *Proc. of the ICML*, Vol. 30, 3 pp.

Peng, Z., and Y. Ben-Zion (2004). Systematic analysis of crustal anisotropy along the Karadere—Düzce branch of the North Anatolian fault, *Geophys. J. Int.* **159,** no. 1, 253–274, doi: 10.1111/j.1365-246X.2004.02379.x.

Perol, T., M. Gharbi, and M. Denolle (2018). Convolutional neural network for earthquake detection and location, *Sci. Adv.* **4,** no. 2, e1700578, doi: 10.1126/sciadv.1700578.

Savage, M. K., A. Wessel, N. A. Teanby, and A. W. Hurst (2010). Automatic measurement of shear wave splitting and applications to time varying anisotropy at Mount Ruapehu volcano, New Zealand, *J. Geophys. Res.* **115,** no. B12, doi: 10.1029/2010JB007722.

Shorten, C., and T. M. Khoshgoftaar (2019). A survey on image data augmentation for deep learning, *J. Big Data* **6,** no. 1, 1–48, doi: 10.1186/s40537-019-0197-0.

Silver, D., A. Huang, C. J. Maddison, A. Guez, L. Sifre, G. Van Den Driessche, J. Schrittwieser, I. Antonoglou, V. Panneershelvam, M. Lanctot, *et al.* (2016). Mastering the game of Go with deep neural networks and tree search, *Nature* **529,** no. 7587, 484–489, doi: 10.1038/nature16961.

Silver, P. G., and W. W. Chan (1991). Shear wave splitting and subcontinental mantle deformation, *J. Geophys. Res.* **96,** no. B10, 16,429–16,454, doi: 10.1029/91JB00899.

Teanby, N. A., J. M. Kendall, and M. Van der Baan (2004). Automation of shear-wave splitting measurements using cluster analysis, *Bull. Seismol. Soc. Am.* **94,** no. 2, 453–463, doi: 10.1785/0120030123.

Yang, Z., A. Sheehan, and P. Shearer (2011). Stress-induced upper crustal anisotropy in southern California, *J. Geophys. Res.* **116,** no. B2, doi: 10.1029/2010JB007655.

Zhang, Y., and S. S. Gao (2022). Classification of teleseismic shear wave splitting measurements: A convolutional neural network approach, *Geophys. Res. Lett.* **49,** no. 12, e2021GL097101, doi: 10.1029/2021GL097101.

Zhu, W., and G. C. Beroza (2019). PhaseNet: A deep-neural-network-based seismic arrival-time picking method, *Geophys. J. Int.* **216,** no. 1, 261–273, doi: 10.1093/gji/ggy423.

Manuscript received 6 December 2023
Published online 8 July 2024

Downloaded from http://pubs.geoscienceworld.org/ssa/srl/article-pdf/doi/10.1785/0220230410/6544270/srl-2023410.1.pdf
by Missouri University of Science and Technology, Stephen Shangxing Gao